HHS Public Access

Author manuscript

Proc SPIE Int Soc Opt Eng. Author manuscript; available in PMC 2010 May 04.

Published in final edited form as:

Proc SPIE Int Soc Opt Eng. 2010 January 24; 7569: 756918. doi:10.1117/12.841017.

Multiphoton microscopy as a diagnostic imaging modality for lung cancer

Ina Pavlova[1], **Kelly R. Hume**[2], **Stephanie A. Yazinski**[2], **Rachel M. Peters**[2,3], **Robert S. Weiss**[2], and **Watt W. Webb**[1]

[1]School of Applied and Engineering Physics, Cornell University, Ithaca, NY

[2]Department of Biomedical Sciences, College of Veterinary Medicine, Cornell University, Ithaca, NY

[3]Section of Pathology, College of Veterinary Medicine, Cornell University, Ithaca, NY

Abstract

Lung cancer is the leading killer among all cancers for both men and women in the US, and is associated with one of the lowest 5-year survival rates. Current diagnostic techniques, such as histopathological assessment of tissue obtained by computed tomography guided biopsies, have limited accuracy, especially for small lesions. Early diagnosis of lung cancer can be improved by introducing a real-time, optical guidance method based on the *in vivo* application of multiphoton microscopy (MPM). In particular, we hypothesize that MPM imaging of living lung tissue based on two-photon excited intrinsic fluorescence and second harmonic generation can provide sufficient morphologic and spectroscopic information to distinguish between normal and diseased lung tissue. Here, we used an experimental approach based on MPM with multichannel fluorescence detection for initial discovery that MPM spectral imaging could differentiate between normal and neoplastic lung in *ex vivo* samples from a murine model of lung cancer. Current results indicate that MPM imaging can directly distinguish normal and neoplastic lung tissues based on their distinct morphologies and fluorescence emission properties in non-processed lung tissue. Moreover, we found initial indication that MPM imaging differentiates between normal alveolar tissue, inflammatory foci, and lung neoplasms. Our long-term goal is to apply results from *ex vivo* lung specimens to aid in the development of multiphoton endoscopy for *in vivo* imaging of lung abnormalities in various animal models, and ultimately for the diagnosis of human lung cancer.

1. Introduction

Lung cancer is the second most common type of cancer in men and women and is the leading cause of cancer-related deaths for both sexes [1]. The disease is usually detected as soft tissue opacities in the lung by thoracic radiography or computed tomography (CT) scans. These abnormal sites are then evaluated for neoplastic cells via fine needle aspirates or biopsies for cytopathologic or histopathologic evaluation. While on average these techniques have a sensitivity and specificity above 90% for the diagnosis of lung cancer[2], they are associated with some significant limitations. Small nodules (less than 1 cm diameter) have a higher rate of false negative diagnoses[3]. Lung nodules with heterogeneous compositions (e.g., with inflammatory or reactive components in addition to the neoplastic cells) present another diagnostic challenge due to sampling error issues[4], [5]. Imaging the

biopsy site at subcellular resolution prior to tissue removal may help overcome sampling inaccuracies. Moreover, microscopic interrogation may provide morphological or spectral information for on-site, real time differentiation of normal, benign and malignant lung and eventually eliminate the need for more invasive tissue removal.

Recently, confocal and multiphoton excitation endoscopes[6, 7] and microendoscopes[8, 9] have been designed for the *in vivo* microscopic imaging of various disease conditions in hollow and solid internal organs. The diagnostic potential of these techniques depends to a major extent on the ability to provide subcellular resolution imaging of optically scattering tissue without photodamaging the interrogated spot. Multiphoton microscopy (MPM) is currently the preferred microscopy technique for optically scattering tissue imaging due to the deeper penetration depth and the minimized photodamage and photobleaching effects of the near-infrared excitation light[10, 11]. Endogenous two-photon excited fluorescence and second harmonic generation (SHG) signal from living tissue provide subcellular resolution images with sufficient morphological details to be diagnostically useful, as has been demonstrated previously with animal models[12-15] and with *ex vivo* biopsies from human neoplastic urinary bladder and gastrointestinal tract samples[16, 17]. Endogenous two-photon excited fluorescence from cells originates from metabolic indicators such as NADH and flavins, and has a broad emission in the blue-green region[14, 15]. Common endogenous extracellular sources of contrast include SHG from collagen and two-photon excited fluorescence from elastin. The neoplastic process often leads to changes in the extracellular matrix and cellular metabolism and is expected to affect both the fluorescence emission and architectural properties of the optically interrogated tissue. Multiphoton excitation microscopy can visualize both architectural and metabolic changes without the need for tissue removal and processing.

The objective of this study is to determine if MPM imaging enhances the contrast between diseased and normal lung, and to test whether lung neoplasms have distinct morphological and spectral characteristics. Healthy lung is composed of branching conduits that deliver air from the environment to terminal pockets called alveoli where gas exchange occurs. Normal pulmonary alveoli are lined by a single cell layer of squamous type I alveolar cells and cuboidal type II alveolar cells that secrete surfactants. The alveolar septae separates neighboring alveoli and contain elastin and collagen fibers, as well as the capillaries that deliver blood for gas exchange[18]. Previous research shows that at 860 nm excitation, SHG from collagen and fluorescence from elastin are major sources of endogenous contrast in pulmonary tissue from disease free mice imaged *ex vivo* [19]. MPM imaging of frozen human lung at 780 nm excitation confirmed that SHG and two-photon excited fluorescence from fibrous structures in the alveolar septae are major sources of contrast from disease free human alveoli[20]. Macrophages, present in the luminal space of alveoli, are also a source of two-photon excited fluorescence that is red-shifted compared to fluorescence from the alveolar septae and the metabolic indicator NADH[19].

Neoplastic lung tissue may have distinct fluorescence emission properties relative to normal alveoli when imaged by MPM. To test this hypothesis, endogenous two-photon excited fluorescence and SHG of unprocessed normal and neoplastic lung were determined by *ex vivo* imaging of samples obtained from two murine models of lung cancer. Tumorigenesis in

the first model depends on conditional expression of activated K-ras, an oncogene which is mutated in approximately 25% of human lung cancers. In this model, a conditional, activated K-ras allele, LSL-K-ras G12D, is inactive due to the presence of a Stop cassette. Cre-mediated recombination removes the cassette, producing the Lox-K-ras G12D allele that expresses activated K-ras. Intranasal delivery of Cre recombinase to mice using an adenoviral vector induces K-ras G12D expression in scattered cells throughout the lungs, resulting in precursor lesions that progress to malignant neoplasms in a reproducible, temporal sequence that has been well characterized previously [21]. Lungs from Lox-K-ras G12D mice show the presence of atypical adenomatous hyperplasia, which is characterized by the growth of atypical epithelial cells along the alveolar septae, and is proposed to be a precursor of adenocarcinoma. As precursor lesions become larger, atypical cells efface the alveolar lumens and form adenomas and adenocarcinomas. To confirm and extend the findings from the LSL-K-ras G12D model, we also evaluated lung neoplasms in a second mouse model based on transgenic overexpression of Rrm2, a subunit of the enzyme ribonucleotide reductase (RNR) that is a key regulator of *de novo* nucleotide biosynthesis [22]. Tumorigenesis in Rrm2 overexpressing transgenic ($Rrm2^{Tg}$) mice involves a mutagenic mechanism that recapitulates the stochastic nature of tumor development in humans and results in lesions with histopathological resemblance to human adenomas and adenocarcinomas. Here, we describe *ex vivo* MPM imaging of tissue from these models and provide evidence that diseased lung is morphologically and spectrally distinct from surrounding normal tissue. Importantly, the results indicate that MPM imaging is able to distinguish inflammatory and neoplastic changes within the lung, demonstrating the tremendous diagnostic potential of this imaging technology.

2. Materials and Methods

2.1 Mouse models of lung cancer

LSL-K-ras G12D mice were obtained from the Mouse Models of Human Cancer Consortium and backcrossed onto a pure 129SvEv genetic background [21]. To induce Cre-mediated recombination and K-ras activation in the lungs, adult mice were sedated with 0.01ml/gram body weight of 2.5% Avertin (tribromoethanol and tert-amyl alcohol) and were administered 6.7×10^8 PFU of AdenoCre virus [23], diluted in 40 ul of PBS, intranasally. The lungs were harvested 6 to 20 weeks post infection. Wild-type control samples from the LSL-K-ras G12D model were also used. $Rrm2^{Tg}$ mice were maintained on pure FVB or mixed FVB-C57Bl/6 genetic backgrounds as previously described [22]. All animal housing and experimentation was performed in accordance with institutional animal care and use guidelines.

2.2 Sample processing

Mice were euthanized by carbon dioxide asphyxiation. The lung lobes were removed immediately and visually inspected for abnormalities. Normal lung has a uniform pink appearance throughout the surface of the lobes, whereas regions with potential abnormalities may be recognized as white or red discolorations or a disruption in the smooth surface of the lung (Fig 3 A). Sites with abnormal appearance were selected on each lobe and imaged 1-2 hours after euthanasia. All lobes were chilled in PBS and kept on ice until they were imaged.

Immediately after imaging, the lobes were fixed in 4% paraformaldehyde or 10% buffered formalin, and paraffin-embedded. The blocks were sectioned at 6 um and the sections stained with a standard hematoxylin and eosin (H&E) protocol. The orientation of the imaged sample was preserved during paraffin embedding. H&E sections from each imaged sample were obtained from a similar depth and location within the sample as imaged during MPM and compared to MPM images of the unprocessed tissues. Pathological assessment was performed according to guidelines in the Mouse Models of Human Cancers Consortium[24].

2.3 Multiphoton microscopy imaging

Samples were imaged with a custom built multiphoton microscope based on a commercial laser scanning unit (Bio-Rad MRC 1024) and an inverted microscope (Olympus, IX-70). A mode-locked Ti:Sapphire laser (Spectra Physics Tsunami) generated laser pulses at 80MHz and ∼100fs duration. Samples were imaged with an Olympus 20×, 0.75 NA water immersion objective or with an Olympus 40×, 1.4 NA water immersion objective for high-magnification images. The excitation wavelength was 780 nm, with ∼30 mW power at the objective and a scan rate of 3 sec/frame. The emitted autofluorescence and SHG from the samples were captured by three detection channels, each equipped with a bi-alkali photomultiplier tube. The first channel detected emitted signal from 355-425 nm, the second channel captured autofluorescence from 440-500 nm, and the third one detected autofluorescence in the 505-655 nm region. For display purposes, images from each channel were superimposed to create one pseudocolored image. In these merged images, “green” pixels indicate dominant fluorescence in the 440-500 nm range, whereas “red” pixels indicate dominant fluorescence in the 505-655 nm range. Blue color indicates 355-425 nm emission (including SHG centered at 390 nm).

3. Results

3.1 Two-photon excited endogenous fluorescence and SHG patterns of normal lung tissue

In order to assess the ability of multiphoton microscopy to distinguish normal and diseased lung, we first performed *ex vivo* MPM imaging on tumor-free lung from an AdenoCre infected wild-type control mouse (LSL-Kras G12D model) (Figure 1). The overall pattern resembles the structure of normal inflated lung tissue in H&E-stained histological sections, with air-filled alveoli clearly apparent. Strong two-photon excited autofluorescence from granular structures is seen in the MPM images, which we speculate may originate from surfactant produced by type II alveolar cells. These granules appear green, indicating dominant fluorescence in the 455-500 nm range. Two-photon excited emission spectra taken from these granular structures have an emission peak at approximately 490 nm (data not shown), which is different from NADH-based fluorescence emission cited by previous publications on MPM imaging of unprocessed tissue[14,15]. Figure 1 C shows a high-magnification image of the alveoli. Some of the alveoli are lined by fibrous structures with blue color (dominant emission at 355-425 nm), which we speculate may originate from SHG of collagen in the alveolar septa. It should be noted that at 780 nm excitation, normal murine alveoli display relatively little signal from fibrous structures. However, in similar images of normal lung taken at 860 nm excitation, autofluorescence and SHG from the fibrous

connective tissue in the alveolar septae are easily visualized, whereas minimal granular fluorescence is displayed (data not shown). These results are similar to those reported in a previous study of MPM imaging of unprocessed normal mouse lung[19]. Taken together, these findings indicate that MPM imaging permits visualization of alveolar structure in unprocessed living lung tissue samples and establish a baseline fluorescent emission pattern for normal lung tissue.

3.2 Distinct two-photon excited endogenous fluorescence and SHG patterns distinguish inflammatory foci, benign neoplasms, and normal lung tissue

Lipid pneumonia is an inflammatory condition that occurs in laboratory mice. It is characterized by the multifocal or diffuse accumulation of large numbers of foamy macrophages and other inflammatory cells within the lumen of the alveoli. The macrophages have lipid or lipofuscin filled vacuoles in their cytoplasm, easily recognized in H&E sections. Figure 2 B shows an MPM image of a region of lipid pneumonia from a 14 month old $Rrm2^{Tg}$ mouse. Large lipid-filled macrophages are seen in the lumen of the alveoli with an orange/red color indicating dominant fluorescence in the 505-655 nm range. This results in a distinct red-shifted fluorescence emission from the site with macrophage infiltration, whereas tissue around the site with macrophage infiltration has the green appearance (dominant fluorescence in the 440-500 nm range) and morphology similar to the example of normal lung displayed in Figure 1 B. The distinct morphological appearance and red-shifted fluorescence of the lipid-filled macrophages suggests that MPM with three-channel detection can readily distinguish sites with macrophage infiltration from normal lung alveoli. An MPM image from the center of a benign neoplasm (adenoma) from an 8.5 month old $Rrm2^{Tg}$ mouse is shown in Figure 3 C. The lung tissue surrounding the nodule shows considerable macrophage infiltration (Fig 3F). The adenoma in this example is characterized by a solid aggregation of cells that disrupt the normal pulmonary architecture, while the tissue surrounding the nodule has well defined alveoli, albeit with macrophage infiltration. Moreover, the adenoma has a blue/cyan appearance, indicating blue-shifted fluorescence compared to normal pulmonary parenchyma (Fig 1B) and the tissue surrounding the adenoma (Fig 3F). Macrophages in the alveoli surrounding the adenoma (Fig 3F) and lipid-filled macrophages from the lipid pneumonia example (Fig 2B) have an orange/red appearance (dominant emission in the 505-655 nm range). Therefore, the spectral appearance of the sites with macrophage infiltration is red-shifted relative to the spectral appearance of the adenoma (and normal alveoli, Fig 1B). The distinct morphological and spectral appearance of the adenoma indicates that MPM imaging with three-channel detection has the potential to distinguish a benign neoplasm from both normal alveolar structures and inflammatory lung sites with extensive macrophage infiltration.

4. Conclusion

In this study, we show that MPM imaging of *ex vivo* samples from two different murine models of lung cancer can be used to differentiate between normal and abnormal lung. Current results indicate that MPM of endogenous fluorescence and SHG provide significant contrast between diseased lung and the surrounding normal alveoli in lung samples imaged *ex vivo*. Specifically, we show that MPM with three-channel detection differentiates lung

lesions with nonmalignant changes (such as pneumonia) from benign neoplastic lesions (such as adenomas).

MPM images from normal mouse lung closely resemble the normal tissue morphology visualized in H&E images, the current gold standard for clinical diagnosis. At 780 nm excitation, the brightest endogenous fluorescence from normal lung originated from granular structures, which may be surfactant complexes secreted from type II alveolar cells. Emission spectra at 780 nm excitation taken from these granular structures displayed a peak at approximately 490 nm, which suggests that the fluorophores responsible for this signal differ from the metabolic indicators NADH and flavins[14, 15]. In addition, thin fibers were observed to surround some of the alveoli and are likely to represent collagen fibers in the alveolar septae. It should be noted that at 780 nm excitation, normal murine alveoli display little fibrous fluorescence in comparison to fluorescence from the granular structures. This pattern contrasts results from a study of liquid nitrogen frozen human lung tissue, where it was found that MPM imaging of normal pulmonary parenchyma at 780 nm excitation shows fluorescence and SHG originating predominantly from the fibrotic connective tissue of the alveolar septae[20]. Aside from the distinct species of origin, a possible reason for this difference is that freezing and thawing of tissue prior to imaging may decrease fluorescence from the molecules responsible for the granular signal observed in the unprocessed mouse lung. In contrast to the pattern of normal lung, lung adenomas manifested as solid aggregations of cells that distorted the normal morphology of the lung. At 780 nm excitation, fluorescence from the adenoma was blue-shifted compared to the fluorescence from normal alveoli. The metabolic indicator NADH is a common source of endogenous contrast from metabolically active cells[14] and could be the dominant fluorophore responsible for the blue-shifted fluorescence from the adenoma. Macrophages in the tissue surrounding the adenoma had a red-shifted fluorescence compared to the tumor cells. Similar fluorescence was also displayed by the macrophage infiltration in the case of lipid pneumonia, which suggests that inflammatory sites with macrophage infiltration could be distinguished from other abnormal lung conditions based on this characteristic red-shifted fluorescence. Porphyrin and lipofuscin, found in the vacuoles of macrophages, are fluorophores with dominant emission in the 505 to 655 nm range[12, 14] and are likely to be responsible for the red-shifted fluorescence in the MPM images of inflammatory sites.

Results from this research demonstrate that *ex vivo* MPM images show morphological and spectral contrast between normal and abnormal lung. In addition, the data suggest that MPM imaging can discriminate between particular lesion types. Further imaging studies of tissue from murine models of lung cancer are needed to determine the morphological and spectral properties of lung masses at different stages of neoplastic transformation. Our long-term goal is to apply results from *ex vivo* imaging of lung specimens to aid in the development of multiphoton microscopic microendoscopy for *in vivo* imaging of lung abnormalities in animal models, and ultimately for the diagnosis of human lung cancer. *In vivo* applications of MPM via microendoscopy using GRIN lenses could address current *in situ* diagnostic challenges by providing microanatomical and/or spectroscopic data for diagnosis of the interrogated tissue site prior to tissue removal. This technology also could be used to guide

needle biopsy procedures to increase the accuracy of tissue sampling and to aid in the assessment of surgical margins during the resection of malignant tissue.

Acknowledgments

These studies were funded in part through NIH grants CA108773 (RSW) and EB006736 (IP and WWW). KRH was supported by a clinical fellowship from the Cornell University College of Veterinary Medicine. SAY was supported by a DOD Breast Cancer Research Program predoctoral fellowship. Editorial help from Mark Williams is greatly appreciated.

References

1. Jemal A, Siegel R, Ward E, Hao YP, Xu JQ, Murray T, Thun MJ. Cancer statistics, 2008. Ca-Cancer J Clin. 2008; 58:71–96. [PubMed: 18287387]
2. Schreiber G, McCrory DC. Performance characteristics of different modalities for diagnosis of suspected lung cancer - Summary of published evidence. Chest. 2003; 123:115S–128S. [PubMed: 12527571]
3. Montaudon M, Latrabe V, Pariente A, Corneloup O, Begueret H, Laurent F. Factors influencing accuracy of CT-guided percutaneous biopsies of pulmonary lesions. Eur Radiol. 2004; 14:1234–1240. [PubMed: 14963689]
4. Meyer C. Transthoracic Needle Aspiration Biopsy of Benign and Malignant Lung Lesions—A Commentary. AJR. 2007; 188:891–893. [PubMed: 17377018]
5. Khouri NF, Stitik FP, Erozan YS, Gupta PK, Kim WS, Scott WW, Hamper UM, Mann RB, Eggleston JC, Baker RR. Transthoracic needle aspiration biopsy of benign and malignant lung lesions. AJR. 1985; 144:281–288. [PubMed: 3871271]
6. Kiesslich R, Goetz M, Neurath MF. Confocal laser endomicroscopy for gastrointestinal diseases. Gastrointestinal Endoscopy Clinics of North America. 2008; 18(3):451–66. [PubMed: 18674696]
7. Myaing MT, MacDonald DJ, Li X. Fiber-optic scanning two-photon fluorescence endoscope. Opt Lett. 2006; 31:1076–1078. [PubMed: 16625908]
8. Levene MJ, Dombeck DA, Molloy RP, Kasischke KA, Williams RM, Zipfel WR, Webb WW. In vivo multiphoton microscopy of deep brain tissue. Journal of Neurophysiology. 2004; 91:1908–1912. [PubMed: 14668300]
9. Barretto RPJ, Messerschmidt B, Schnitzer MJ. In vivo fluorescence imaging with high-resolution microlenses. Nature Methods. 2009; 6(7):511–512. [PubMed: 19525959]
10. Denk W, Strickler JH, Webb WW. Two-Photon Laser Scanning Fluorescence Microscopy. Science. 1990; 248:73–76. [PubMed: 2321027]
11. Zipfel WR, Williams RM, Webb WW. Nonlinear Magic: Multiphoton Microscopy in the Biosciences. Nature Biotechnology. 2003; 21:1369–1377.
12. Kwan AC, Duff K, Gouras GK, Webb WW. Optical visualization of Alzheimer's pathology via multiphoton-excited intrinsic fluorescence and second harmonic generation. Opt Express. 2009; 17:3679–3689. [PubMed: 19259208]
13. Kasischke KA, Vishwasrao HD, Fisher PJ, Zipfel WR, Webb WW. Neural activity triggers neuronal oxidative metabolism followed by astrocytic glycolysis. Science. 2004; 305:99–103. [PubMed: 15232110]
14. Zipfel WR, Williams RM, Christie RH, Nikitin AY, Hyman BT, Webb WW. Live Tissue Intrinsic Emission Microscopy Using Multiphoton Excited Intrinsic Fluorescence and Second Harmonic Generation. PNAS. 2003; 100:7075–7080. [PubMed: 12756303]
15. Vishwasrao HD, Heikal AA, Kasischke KA, Webb WW. Conformational Dependence of Intracellular NADH on Metabolic State Revealed by Associated Fluorescence Anisotropy. JBC. 2005; 280(26):25119–25126.
16. Mukherjee S, Wysock JS, Ng CK, Akhtar M, Perner S, Lee MM, Rubin MA, Maxfield FR, Webb WW, Scherr DS. Human bladder cancer diagnosis using Multiphoton microscopy. Proceedings of SPIE. 2009; 7161:716117-716111–716117-716110.

17. Rogart JN, Nagata J, Loeser CS, Roorda RD, Aslanian H, Robert ME, Zipfel WR, Nathanson MH. Multiphoton imaging can be used for microscopic examination of intact human gastrointestinal mucosa ex vivo. Clin Gastroenterol Hepatol. 2008; 6:95–101. [PubMed: 18065276]

18. Conti CJ. Atlas of Laboratory Mouse Histology. 2009http://ctrgenpath.net/atlas/mouseHistology

19. Pena A, Fabre A, Debarre D, Marchal-Somme J, Crestani, Martin J, Beaurepaire E, Schanne-Klein M. Three-Dimensional investigation and scoring of extracellular matrix remodeling during lung fibrosis using multiphoton microscopy. Microscopy Research and Technique. 2007; 70:162–170. [PubMed: 17177275]

20. Wang CC, Li FC, Wu RJ, Hovhannisyan VA, Lin WC, Lin SJ, So PTC, Dong CY. Differentiation of normal and cancerous lung tissues by multiphoton imaging. Journal of Biomedical Optics. 2009; 14(4):044034. [PubMed: 19725745]

21. Xu X, Page JL, Surtees JA, Liu HC, Lagedrost S, Li Y, Bronson R, Alani E, Nikitin AY, Weiss RS. Broad overexpression of ribonucleotide reductase genes in mice specifically induces lung neoplasms. Cancer Res. 2008; 68:2652–2660. [PubMed: 18413732]

22. Jackson EL, Willis N, Mercer K, Bronson RT, Crowley D, Montoya R, Jacks T, Tuveson DA. Analysis of lung tumor initiation and progression using conditional expression of oncogenic K-ras. Genes Dev. 2001; 15:3243–3248. [PubMed: 11751630]

23. Nikitin AY, Alcaraz A, Anver MR, Bonson RT, Cardiff RD, Dixon D, Fraire AE, Gabrielson EW, Gunning WT, Haines DC, Kaufman MH, Linnoila RI, Maronpot RR, Rabson AS, Reddick RL, Rehm S, Rozengurt N, Schuller HM, Shmidt EN, Travis WD, Ward JM, Jacks T. Classification of proliferative pulmonary lesions of the mouse: Recommendations of the mouse models of human cancers consortium. Cancer Res. 2004; 64:2307–2316. [PubMed: 15059877]

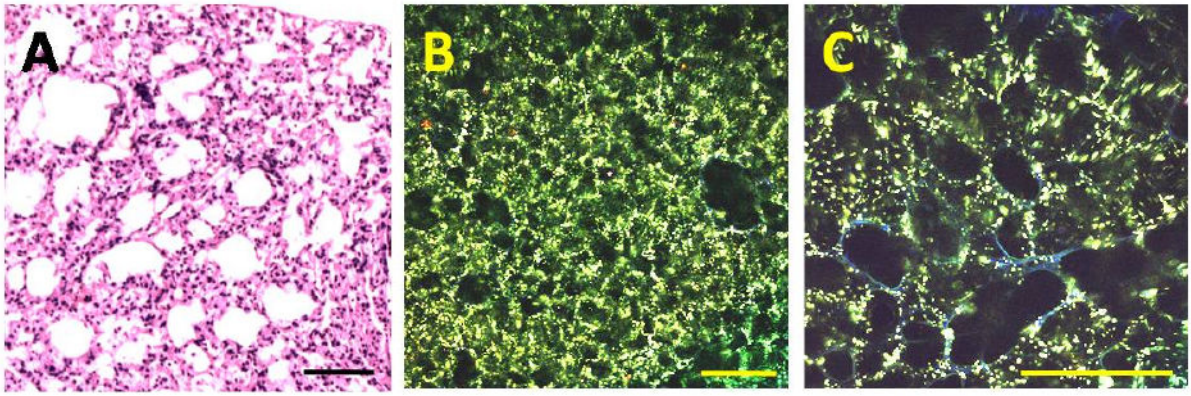

Figure 1.

MPM imaging of tumor-free murine lung showing normal alveolar structure. The sample was collected from an AdenoCre infected wild-type control mouse from the LSL-Kras G12D model. After imaging, the sample was fixed in 4% paraformaldehyde, and embedded, sectioned, and stained with H&E (A). (B) Low-magnification MPM image showing the overall morphology of the sample. Note that the MPM and H&E image are from comparable but not identical regions. (C) High-magnification MPM image showing individual alveoli. Two-photon fluorescence and SHG were excited at 780 nm and detected at 355-425 nm, 440-500 nm and 505-655 nm emission bands. The displayed MPM images were generated by superimposing the individual images from the three bands; blue color indicates dominant emission at 355-425 nm; green color represents fluorescence in the 440-500 nm region. Scale bar: 100um.

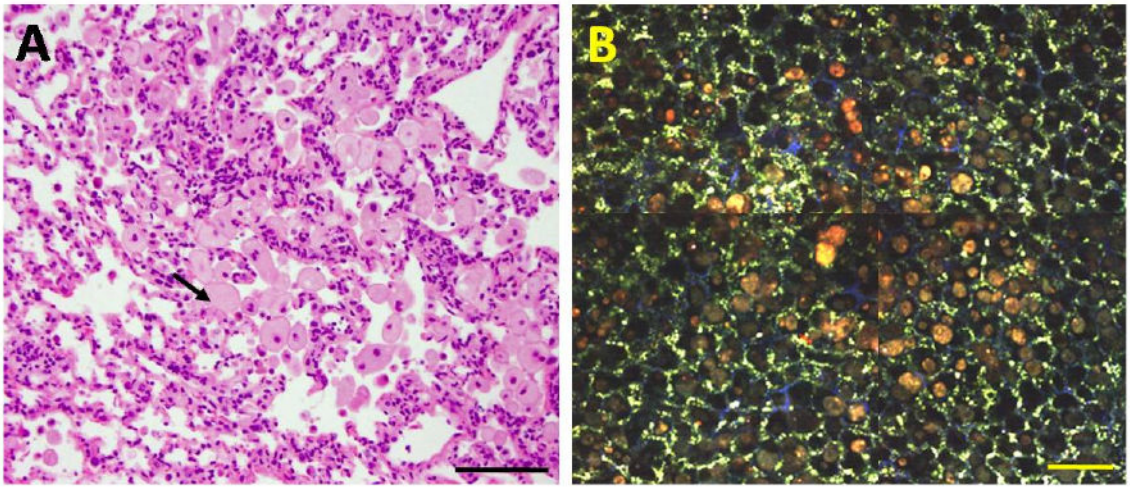

Figure 2.

MPM imaging of lipid pneumonia in murine lungs. The sample was collected from a 14 month old $Rrm2^{Tg}$ mouse with a small white mass visible on the lung surface at necropsy. After imaging, the sample was fixed in 10% buffered formalin, and then embedded, sectioned, and stained with H&E (A). A series of MPM images was collected and assembled into a mosaic composite (B). The MPM and H&E images are from similar but not identical regions of the sample. Two-photon fluorescence and SHG were excited at 780 nm and detected at 355-425 nm, 440-500nm and 505-655 nm emission bands. In the displayed superimposed images blue color indicates emission at 355-425 nm; green color represents fluorescence at 440-500 nm; and red color indicates fluorescence at 505-655 nm. The black arrow in (A) points to a lipid-filled macrophage, characteristic of lipid pneumonia in mice. Scale bar: 100um.

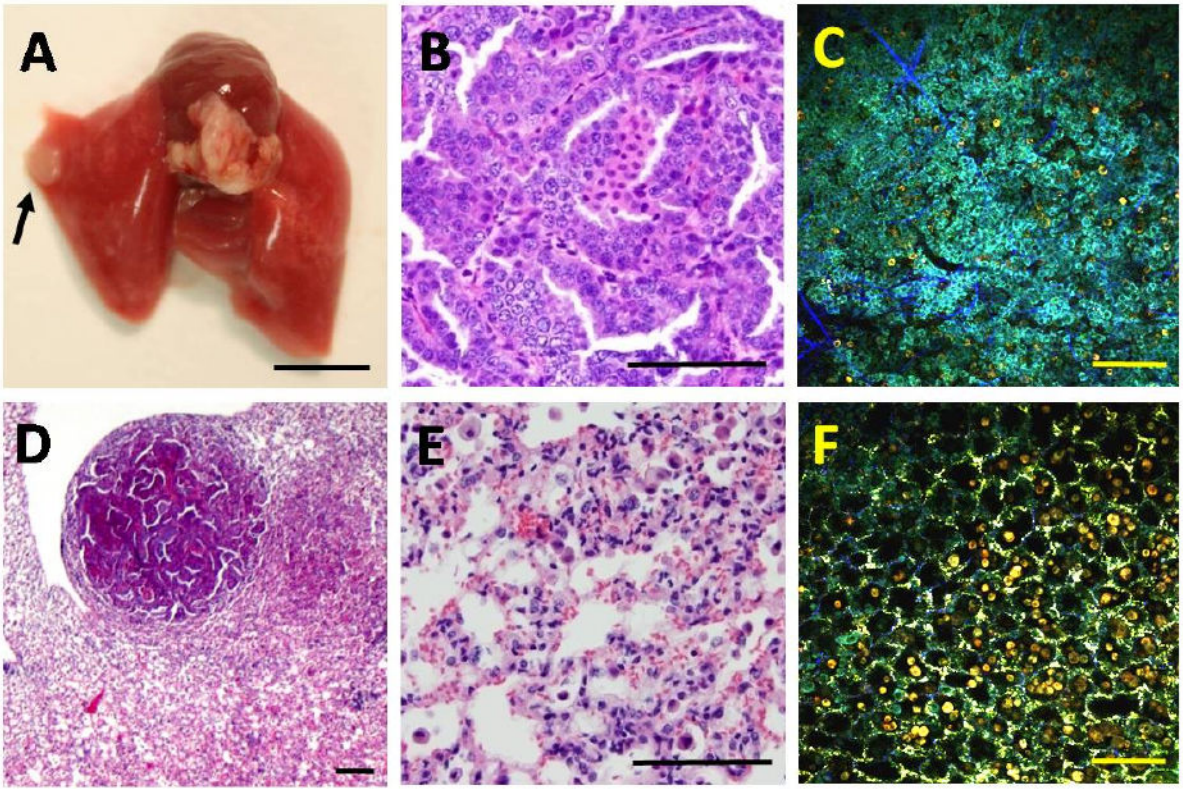

Figure 3.

MPM imaging of a benign lung adenoma. The sample was taken from an 8.5 month old $Rrm2^{Tg}$ mouse. A white mass was visible on the lung surface at necropsy (A) and was identified as an adenoma in H&E sections imaged at high- (B) or low- (D) magnification. MPM and H&E images were generated at the center of the adenoma (B,C) or at an adjacent non-neoplastic site (E,F) with marked macrophage infiltration. The MPM (C,F) and H&E (B,E) images are from similar but not identical regions of the sample. The black arrow in (A) points to the location of the adenoma. The scale bar: 5000um in (A) and 100um in (B-F).